

Collective excitations and screening in two-dimensional tilted nodal-line semimetals

Hamid Rahimpour¹ and Saeed H. Abedinpour^{1*}

Department of Physics, Institute for Advanced Studies in Basic Sciences (IASBS), Zanjan 45137-66731, Iran



(Received 21 September 2023; accepted 20 December 2023; published 10 January 2024)

Topological nodal-line semimetals are characterized by symmetry-protected one-dimensional band-touching lines or loops, which give rise to their peculiar Fermi surfaces at low energies. Furthermore, if time reversal or inversion symmetry breaking tilts the bands, anisotropic Fermi surfaces simultaneously hosting electron and hole carriers can also appear. We analytically investigate the linear density-density response function of a two-dimensional tilted nodal-line semimetal in the intrinsic and doped regimes. Despite the anisotropic electronic bands, the polarizability remains isotropic in our model system. We find that the plasmon dispersion in the long-wavelength limit exhibits a standard behavior proportional to the wave vector's square root, characteristic of two-dimensional electron liquids. Tilting enhances the plasmon frequency, and the Drude weight does not depend on the carrier density at low doping levels. Unlike the intrinsic and highly doped systems, static polarizability has two distinct singularities at finite wave vectors in the low doped regimes. These two singularities result in beat patterns in the Friedel oscillations.

DOI: [10.1103/PhysRevB.109.045120](https://doi.org/10.1103/PhysRevB.109.045120)

I. INTRODUCTION

Topological phases of matter are an emerging subject in modern condensed-matter physics that has sparked considerable interest in the past two decades. Even though the starting point of these topological materials was topological insulators characterized by their gapped bulk electronic energy spectrum and symmetry-protected gapless surface states [1–3], gapless topological materials have been gaining significant attention lately. These appealing materials are known as topological semimetals, they possess zero-gap bulk states [4,5], and they may also support nontrivial surface states. In topological semimetals, the valence and conduction bands touch each other either in isolated points or along open or closed lines in the Brillouin zone (BZ). The topological band crossing in the bulk is either accidental or symmetry-enforced [6]. The low-energy excitations around the nodal points are described by the massless Dirac equation [7–10], with the representative examples being Na_3Bi [11] and Cd_3As_2 [12] for the Dirac semimetals, as well as TaAs [13] and TaP [14] for the Weyl semimetals. Breaking the time-reversal or inversion symmetry in Dirac semimetal results in a Weyl semimetal with twofold-degenerate point nodes in momentum space [5].

Dirac cones in Dirac or Weyl semimetals might be tilted [15,16], and several interesting phenomena are associated with that [17–20]. These tilted semimetals are usually classified according to the geometry of their Fermi surfaces. For instance, in so-called type-II Weyl semimetals, overtilted Dirac cones give rise to particle and hole pockets at the intersection of the Dirac cone with the Fermi level [15].

In another family of topological semimetals, namely nodal-line semimetals (NLSMs), band crossing takes place along a

line or closed loop in the BZ [21,22]. A large variety of material candidates are proposed for NLSMs. Cu_3PdN [23] and CaAgAs [24] are among the vast number of theoretical candidates, whereas ZrSiS [25,26], NbAs_2 [27], and YbMnSb_2 [28] are examples of experimentally validated three-dimensional (3D) NLSMs. Similar to Dirac cones, the nodal line can be tilted too, due to time reversal or inversion symmetry breaking. Such tilted nodal lines are observed in several materials, including ZrSiS , HfSiS , and ZrSiSe [29,30].

Nodal-line semimetals are investigated in two dimensions as well. Jin *et al.* predicted a family of two-dimensional (2D) nodal-line semimetals MX with $M = \text{Pd, Pt}$, and $X = \text{S, Se, Te}$ [31] using an evolutionary algorithm and first-principles calculations, and Lu *et al.* suggested a possible realization of 2D NLSMs in a mixed honeycomb-kagomé lattice structure [32]. A Lieb lattice structure for compounds like Be_2C and BeH_2 is also suggested as a feasible candidate for robust two-dimensional NLSMs [33,34]. Time-reversal or inversion symmetry breaking can induce band tilting in two dimensions, too.

Various properties of different types of NLSMs have been extensively explored so far (see, e.g., Ref. [6], and references therein). Optical conductivity [35,36] and thermoelectric responses [37] of two- and three-dimensional NLSMs are investigated. As for the collective excitations, the plasmon frequency of 3D NLSMs at long wavelength shows an $n^{1/4}$ dependence on the carrier density n , which is distinct from the ordinary electron liquids, and Dirac or Weyl semimetals [38]. The Friedel oscillations in 3D NLSMs exhibit an angle-dependent algebraic power-law decay [39]. Also, a recent study [40] of the collective modes of a 2D nonsymmorphic NLSM with an open band-touching line predicts a strongly anisotropic plasmon dispersion in these materials.

This paper considers an effective low-energy two-band Hamiltonian with a circular nodal loop and a linear tilt term.

*abedinpour@iasbs.ac.ir

We investigate the zero-temperature linear density-density response function in the static and dynamic regimes at different carrier concentration levels of this system. The rest of this paper is organized as follows. Section II introduces the low-energy effective Hamiltonian of a 2D tilted NLSM and discusses its different doping regimes. In Sec. III, we analytically calculate the imaginary and real parts of the linear density-density response function in the intrinsic and doped regimes. The static limit behavior and screening of the charged impurity are discussed in Sec. IV, while Sec. V is devoted to a discussion of the collective density mode and the behavior of plasmon frequency at long wavelength as well as arbitrary wave vectors within the random phase approximation (RPA). We conclude and summarize our main findings in Sec. VI. Finally, Appendix A illustrates the steps for obtaining an effective two-band continuum model Hamiltonian of a 2D NLSM from the tight-binding model of a Lieb lattice, and in Appendix B we present the details of calculating the dynamical polarizability.

II. MODEL HAMILTONIAN

We consider the following effective low-energy single-particle model Hamiltonian, for a two-dimensional semimetal with a circular nodal line and linear tilt ($\hbar = 1$) [41,42]:

$$\hat{H}_0 = \mathbf{u} \cdot \mathbf{k} \hat{\tau}_0 + \frac{1}{2m} (k^2 - k_0^2) \hat{\tau}_x. \quad (1)$$

Here, \mathbf{u} is the tilt velocity vector, $\hat{\tau}_0$ and $\hat{\tau}_x$ are, respectively, the two by two identity matrix and x -component of the Pauli matrix, acting on the pseudospin (i.e., orbital) degree of freedom, m is the band mass, $k = |\mathbf{k}| = \sqrt{k_x^2 + k_y^2}$ is the magnitude of the wave vector, and k_0 is the radius of the nodal loop in the absence of tilt. Note that we can arrive at the effective Hamiltonian (1) from the low-energy limit of tight-binding models. For an example of such models in a Lieb lattice, see Appendix A. The linear tilt term can have different origins. A feasible scenario is an in-plane electric field that breaks the inversion symmetry and induces spin-orbit coupling (SOC). Such a SOC tilts two spin subbands in opposite directions (see Appendix A for details). As our results are independent of the tilt direction and real spin degree of freedom, in the following we will work with the simple spin-independent Hamiltonian of Eq. (1).

Eigenvalues corresponding to Hamiltonian (1) are given by

$$\varepsilon_{\mathbf{k},s} = \mathbf{u} \cdot \mathbf{k} + s \frac{|k^2 - k_0^2|}{2m}, \quad (2)$$

where $s = +(-)$ labels the conduction (valence) band. Moreover, the eigenstates of our model Hamiltonian are readily obtained as

$$|\mathbf{k}, s\rangle = \frac{1}{\sqrt{2}} \begin{pmatrix} 1 \\ s \operatorname{sgn}(k^2 - k_0^2) \end{pmatrix}. \quad (3)$$

Here, $\operatorname{sgn}(x)$ is the sign function. The tilt term considered in Eq. (1) does not affect the eigenstates, and in the $\mathbf{u} \rightarrow \mathbf{0}$ limit we recover the model Hamiltonian for untilted 2D NLSMs [35]. It is worth noting that in the BZ of real materials, tilted nodal lines should appear in pairs of opposite tilt velocities, either at the same point or at different valleys in the BZ.

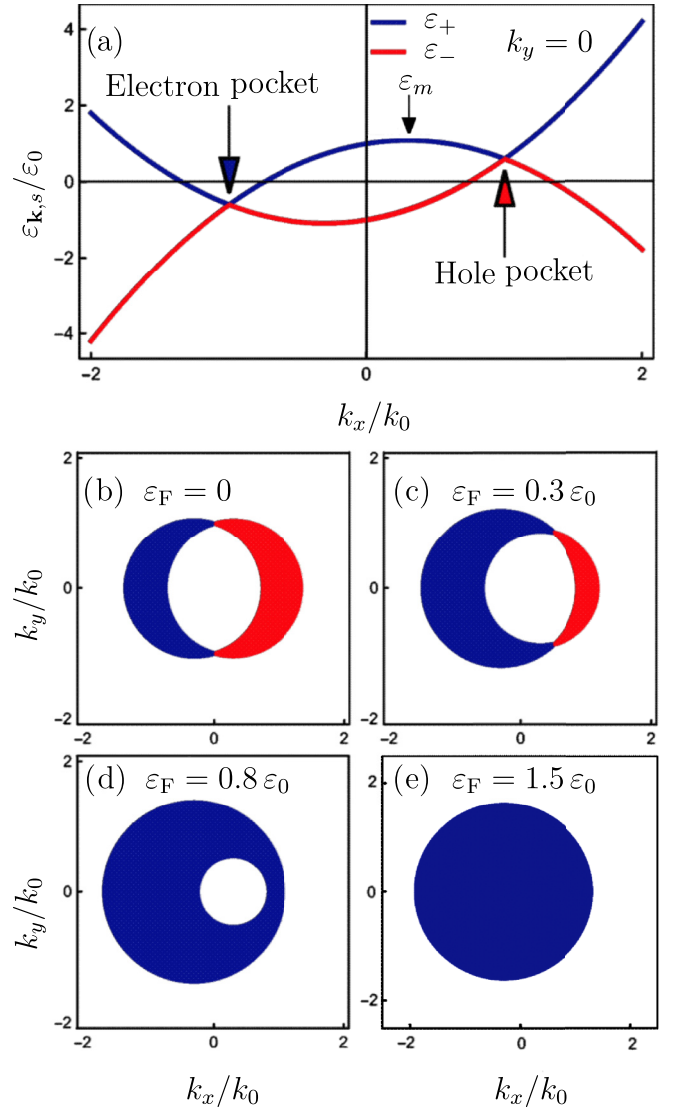


FIG. 1. (a) Low-energy spectrum of a 2D tilted NLSM [in units of $\varepsilon_0 = k_0^2/(2m)$], vs k_x/k_0 for $k_y = 0$. (b)–(e) Fermi surfaces for (b) $\varepsilon_F = 0$, (c) $\varepsilon_F = 0.3 \varepsilon_0$, (d) $\varepsilon_F = 0.8 \varepsilon_0$, and (e) $\varepsilon_F = 1.5 \varepsilon_0$. Electron and hole portions of the Fermi surfaces are identified by blue and red, respectively. We have fixed the tilt velocity at $u = 0.3 v_0$, with $v_0 = k_0/m$ in all plots.

As we will see later, our results are independent of the tilt direction; therefore, additional nodal lines will contribute to the degeneracy factor. In the following, without losing the generality of our problem, we will take the tilt along the x direction and set $u_y = 0$.

In Fig. 1, panel (a) shows the energy dispersion of a 2D tilted NLSM, and panels (b)–(e) illustrate the Fermi surfaces for the intrinsic (i.e., undoped) system and for different doping values. A finite tilt rotates the band-touching circle around the y -axis, partially lifting the valence band into positive energies and pushing down the conduction band into negative energies. This rotation leads to the simultaneous appearance of electron and hole pockets at the Fermi levels in the intrinsic and low-doped systems. We can readily find the density of states per unit area (DOS) from the energy dispersions,

$\rho(\varepsilon) = \rho_0[2 - \Theta(|\varepsilon| - \varepsilon_m)]$, where $\rho_0 = gm/(2\pi)$ is the DOS of an ordinary 2D electron gas [43], with g the total degeneracy factor, $\Theta(x)$ is the Heaviside step function, and $\varepsilon_m = \varepsilon_0(1 + u^2/v_0^2)$, where $v_0 = k_0/m$ is the energy corresponding to the extremum point of the conduction band, and $\varepsilon_0 = k_0^2/(2m)$. Note that the Fermi surface becomes a full disk for $|\varepsilon_F| > \varepsilon_m$, where ε_F is the Fermi energy [see Fig. 1, panel (e)]. Considering only electron-doped (i.e., $\varepsilon_F > 0$) systems, just for the sake of definiteness, we can easily find the Fermi energy in terms of the extra carrier density

$$\varepsilon_F = \begin{cases} n_e/(2\rho_0), & n_e \leq n_m, \\ (n_e/\rho_0) - \varepsilon_m, & n_e > n_m, \end{cases} \quad (4)$$

where n_e is the doped carrier concentration, measured with respect to the intrinsic limit, i.e., $\varepsilon_F = 0$, and $n_m = 2\rho_0\varepsilon_m$ is the density at $\varepsilon_F = \varepsilon_m$.

III. NONINTERACTING DENSITY-DENSITY RESPONSE FUNCTION

When an electronic system is subjected to an external electromagnetic perturbation, the charge distribution changes, and the system becomes polarized. The noninteracting density-density response function, or the polarizability of a 2D NLSM, is given by the bare bubble diagram [43]

$$\Pi(\mathbf{q}, \omega) = \frac{g}{S} \sum_{\mathbf{k}ss'} F_{ss'}(\mathbf{k}, \mathbf{k}') \frac{f(\varepsilon_{\mathbf{k},s}) - f(\varepsilon_{\mathbf{k}',s'})}{\hbar\omega + \varepsilon_{\mathbf{k},s} - \varepsilon_{\mathbf{k}',s'} + i0^+}, \quad (5)$$

where S is the sample area, $\mathbf{k}' = \mathbf{k} + \mathbf{q}$, $f(\varepsilon) = 1/[\exp(\beta(\varepsilon - \mu)) + 1]$ is the Fermi-Dirac distribution function, with $\beta = 1/(k_B T)$ the inverse temperature, μ is the chemical potential, and $F_{ss'}(\mathbf{k}, \mathbf{k}') = |\langle \mathbf{k}, s | \mathbf{k}', s' \rangle|^2 = [1 + ss' \operatorname{sgn}(k^2 - k_0^2) \operatorname{sgn}(k'^2 - k_0^2)]^2/4$ is the form factor obtained from the overlap between eigenstates. Note that this form factor is either 0 or 1.

In the following subsections, we present analytic results for the real and imaginary parts of $\Pi(\mathbf{q}, \omega)$ at different doping regimes and zero temperature, where $f(\varepsilon)|_{T \rightarrow 0} = \Theta(\varepsilon_F - \varepsilon)$.

A. Polarizability of intrinsic 2D NLSM

In an intrinsic NLSM, the Fermi energy is zero, and the imaginary part of $\Pi(\mathbf{q}, \omega)$ reads

$$\operatorname{Im} \Pi(q, \omega) = \frac{2\rho_0 k_0}{q} \sum_{s=\pm 1} s \sqrt{\kappa^2 - v_s^2} \Theta(\kappa^2 - v_s^2), \quad (6)$$

where $\kappa = \sqrt{\varepsilon_m/\varepsilon_0} = \sqrt{1 + u^2/v_0^2}$, and $v_{\pm} = \omega/(v_0 q) \pm q/(2k_0)$.

In Fig. 2, panel (a), the shaded regions show the electron-hole continuum (EHC), where $\operatorname{Im} \Pi(q, \omega)$ is different from zero. $\omega_{\pm} = q^2/(2m) \pm \kappa v_0 q$ separates EHC from $\operatorname{Im} \Pi(q, \omega) = 0$ regions, where single electron-hole excitation is not allowed.

Regions of the EHC labeled as I and II in Fig. 2, panel (a), refer to areas of the ω - q plane defined through

$$\begin{aligned} \text{I: } & v_+^2 < \kappa^2; v_-^2 < \kappa^2, \\ \text{II: } & v_+^2 > \kappa^2; v_-^2 < \kappa^2. \end{aligned} \quad (7)$$

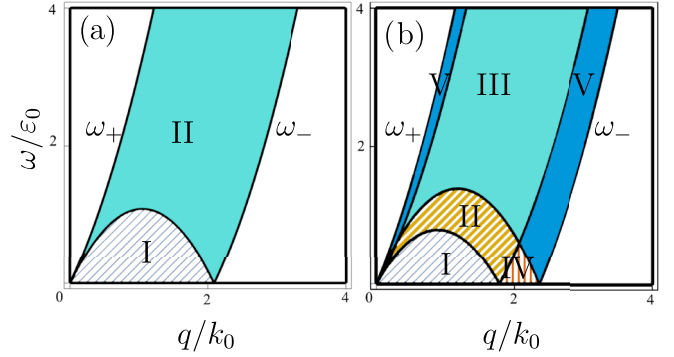


FIG. 2. Electron-hole continuum of a 2D tilted NLSM with $u = 0.3 v_0$, in the intrinsic regime (a), and the low-doped regime with $\varepsilon_F = 0.3 \varepsilon_0$ (b). Different colors point to regions of the ω - q plane with different expressions for the imaginary part of the noninteracting polarizability (see the text for definitions), and $\operatorname{Im} \Pi(q, \omega)$ vanishes in the white regions.

With the help of the Kramers-Kronig relation, we can find the real part of the polarizability

$$\begin{aligned} \operatorname{Re} \Pi(q, \omega) = & -2\rho_0 + \frac{2\rho_0 k_0}{q} \sum_{s=\pm 1} s \operatorname{sgn}(v_s) \\ & \times \sqrt{v_s^2 - \kappa^2} \Theta(v_s^2 - \kappa^2). \end{aligned} \quad (8)$$

B. Polarizability of 2D NLSM at low dopings

For $0 < \varepsilon_F < \varepsilon_m$, the Fermi surface has a hollow in its center. In this regime, analytic expressions for the imaginary and real parts of the zero-temperature density-density linear response function are obtained, respectively, as

$$\operatorname{Im} \Pi(q, \omega) = \frac{\rho_0 k_0}{q} \sum_{s,s'=\pm 1} s \sqrt{\kappa_s'^2 - v_s^2} \Theta(\kappa_s'^2 - v_s^2) \quad (9)$$

and

$$\begin{aligned} \operatorname{Re} \Pi(q, \omega) = & -2\rho_0 + \frac{\rho_0 k_0}{q} \sum_{s,s'=\pm 1} s \operatorname{sgn}(v_s) \\ & \times \sqrt{v_s^2 - \kappa_s'^2} \Theta(v_s^2 - \kappa_s'^2), \end{aligned} \quad (10)$$

where $\kappa_{\pm} = \sqrt{\kappa^2 \pm \varepsilon_F/\varepsilon_0}$.

Panel (b) of Fig. 2 illustrates the EHC of a 2D tilted NLSM in the low-doped regime. Now, the boundaries of the EHC are given by $\omega_{\pm} = q^2/(2m) \pm \kappa_{\pm} v_0 q$. Different regions of the EHC are defined through the following conditions:

$$\begin{aligned} \text{I: } & v_+^2 < \kappa_-^2; v_-^2 < \kappa_+^2; v_-^2 < \kappa_-^2; v_+^2 < \kappa_+^2, \\ \text{II: } & v_+^2 > \kappa_-^2; v_-^2 < \kappa_+^2; v_-^2 < \kappa_-^2; v_+^2 < \kappa_+^2, \\ \text{III: } & v_+^2 > \kappa_-^2; v_-^2 < \kappa_+^2; v_-^2 < \kappa_-^2; v_+^2 > \kappa_+^2, \\ \text{IV: } & v_+^2 > \kappa_-^2; v_-^2 > \kappa_+^2; v_-^2 < \kappa_-^2; v_+^2 < \kappa_+^2, \\ \text{V: } & v_+^2 > \kappa_-^2; v_-^2 > \kappa_+^2; v_-^2 < \kappa_-^2; v_+^2 > \kappa_+^2. \end{aligned} \quad (11)$$

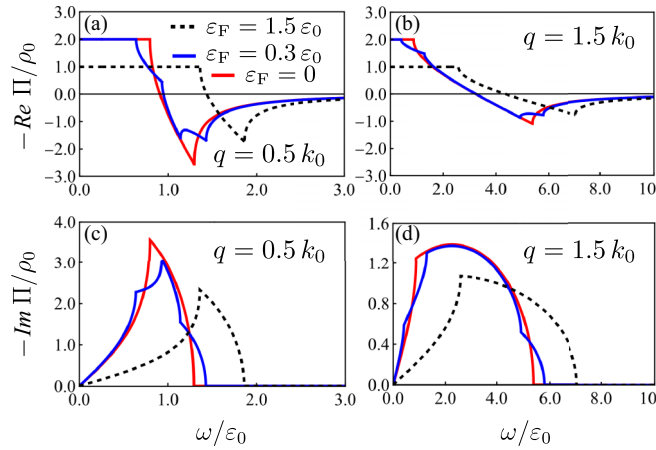


FIG. 3. The real [(a) and (b)] and imaginary [(c) and (d)] parts of the noninteracting dynamical polarizability of a 2D tilted NLSM as a function of ω/ε_0 for $q = 0.5 k_0$ [panels (a) and (c)] and $q = 1.5 k_0$ [panels (b) and (d)] and for varying Fermi energies. The Fermi energies $\varepsilon_F = 0$, $\varepsilon_F = 0.3 \varepsilon_0$, and $\varepsilon_F = 2.0 \varepsilon_0$ correspond to the intrinsic, low-doped, and high-doped regimes, respectively. We fixed the tilt velocity at $u = 0.3 v_0$ in all panels.

C. Polarizability of 2D NLSM at high dopings

In the high doping regime, where $\varepsilon_F > \varepsilon_m$, the Fermi surface becomes a filled circle with radius $k_0 \kappa_+$, centered around $(-mu, 0)$ in the k_x - k_y plane. The density-density response in this regime is similar to the intrinsic case. One only needs to substitute κ in Eqs. (6) and (8) with κ_+ and divide the whole expressions with 2, as the density of states, in this case, is half of the undoped system. We write the final expressions here just for the sake of completeness,

$$\text{Im } \Pi(q, \omega) = \frac{\rho_0 k_0}{q} \sum_{s=\pm 1} s \sqrt{\kappa_+^2 - v_s^2} \Theta(\kappa_+^2 - v_s^2), \quad (12)$$

$$\begin{aligned} \text{Re } \Pi(q, \omega) = & -\rho_0 + \frac{\rho_0 k_0}{q} \sum_{s=\pm 1} s \text{sgn}(v_s) \\ & \times \sqrt{v_s^2 - \kappa_+^2} \Theta(v_s^2 - \kappa_+^2). \end{aligned} \quad (13)$$

$$\Pi(q) = -\rho_0 \begin{cases} 2 - 2\Theta(q - 2k_0\kappa)\sqrt{1 - (2k_0\kappa/q)^2}, & \varepsilon_F = 0, \\ 2 - \sum_{s=\pm 1} \Theta(q - 2k_0\kappa_s)\sqrt{1 - (2k_0\kappa_s/q)^2}, & 0 < |\varepsilon_F| < \varepsilon_m, \\ 1 - \Theta(q - 2k_0\kappa_+)\sqrt{1 - (2k_0\kappa_+/q)^2}, & |\varepsilon_F| > \varepsilon_m. \end{cases} \quad (15)$$

In the long-wavelength limit, the static density-density response function is equal to the negative of the density of states at the Fermi level. Another essential characteristic of static polarizability is its singular behavior due to the Fermi surface separating empty and filled states. As Fig. 4 shows, static polarizability of the intrinsic and highly doped systems has singular points at $q = k_0 \kappa$ and $q = k_0 \kappa_+$, respectively. In the low-doping regime, on the other hand, two singularities at $q = k_0 \kappa_{\pm}$ correspond to the radius of inner and outer circles of the Fermi surfaces [see panels (c) and (d) in Fig. 1].

B. Friedel oscillations

The singular points of the static density response function cause Friedel oscillations in the impurity screening. The Fourier transform of the static polarizability, i.e., $\Pi(r) = \int d^2 q \Pi(\mathbf{q}) e^{i\mathbf{q}\cdot\mathbf{r}} / (2\pi)^2$, gives the charge density induced at a distance r from a

It is clear from Eq. (12) that the EHC looks similar to panel (a) of Fig. 2, where the boundaries now depend on the Fermi energy $\omega_{\pm} = q^2/(2m) \pm \kappa_+ v_0 q$, and different regions of the EHC are defined through

$$\begin{aligned} \text{I} : & v_+^2 < \kappa_+^2; v_-^2 < \kappa_+^2, \\ \text{II} : & v_+^2 > \kappa_+^2; v_-^2 < \kappa_+^2. \end{aligned} \quad (14)$$

Figure 3 illustrates the behavior of noninteracting dynamical polarizability $\Pi(q, \omega)$ versus ω for varying wave vectors and doping regimes. In the intrinsic limit, the real part of the polarizability [red curves in panels (a) and (b) of Fig. 3] has a negative plateau for $\omega < \omega_-$, and it changes sign at higher frequencies. The imaginary part of the polarizability [red curves in panels (c) and (d) of Fig. 3] displays a cusp at the boundary between regions I and II of the EHC and vanishes for $\omega > \omega_+$, i.e., beyond the upper edge of the EHC. In the low-doped regime (blue curves in Fig. 3), the polarizability's real and imaginary parts display several distinct cusps corresponding to crossings between different regions within the EHC. The imaginary part vanishes outside the EHC, i.e., for $\omega > \omega_+$. The behavior of $\Pi(\mathbf{q}, \omega)$ in the high-doped regime (dashed black lines), apart from the Fermi energy dependence, is similar to the intrinsic system.

IV. STATIC RESPONSE AND FRIEDEL OSCILLATIONS

In this section, we discuss the behavior of the noninteracting linear density-density response function of a 2D tilted NLSM in the static limit, and we investigate how this system screens charged impurities at different doping regimes.

A. Static polarizability

The static polarizability is a real function, and its analytic form at different dopings is obtained easily from the $\omega \rightarrow 0$ limit of Eqs. (8), (10), and (13), which reads

point impurity potential [43]. Taking the Fourier transforms of Eq. (15), we find

$$\Pi(r) = \frac{8k_0^2 \rho_0}{\pi} \sum_{n=0,1} \begin{cases} 2\kappa^2 J_n(2k_0 \kappa r) N_n(2k_0 \kappa r), & \varepsilon_F = 0. \\ \sum_{s=\pm 1} \kappa_s^2 J_n(2k_0 \kappa_s r) N_n(2k_0 \kappa_s r), & 0 < |\varepsilon_F| < \varepsilon_m. \\ \kappa_+^2 J_n(2k_0 \kappa_+ r) N_n(2k_0 \kappa_+ r), & |\varepsilon_F| > \varepsilon_m, \end{cases} \quad (16)$$

where $J_n(x)$ and $N_n(x)$ are the Bessel functions of the first and second kind, respectively.

It is easy to verify that $\Pi(r)$ decays as r^{-2} at long distances. Furthermore, the Bessel functions give rise to an oscillatory spatial modulation of the induced density. The behavior of $\Pi(r)$ versus r at different Fermi energies is depicted in Fig. 5. The period of oscillations in the intrinsic regime is given by the radius of the nodal ring k_0 . In contrast, the ring radius and the Fermi energy contribute to the doped systems' oscillation period. At low dopings, two distinct singularities of $\Pi(q)$ give rise to the superposition of two oscillating functions with different periods. The resulting beat patterns are evident in panels (b) and (c) of Fig. 5.

V. DRUDE WEIGHT AND PLASMON DISPERSION

In the random phase approximation, the interacting linear density-density response function reads

$$\chi^{\text{RPA}}(q, \omega) = \frac{\Pi(q, \omega)}{\varepsilon^{\text{RPA}}(q, \omega)}. \quad (17)$$

Here, $\varepsilon^{\text{RPA}}(q, \omega) = 1 - v(q)\Pi(q, \omega)$ is the dynamical dielectric function within the RPA, where $v(q) = 2\pi e^2/q$ is the Fourier transform of the Coulomb interaction in 2D, with e the electron charge. Zeros of the dynamical dielectric function (or equivalently, poles of the interacting dynamical polarizability) give the dispersions of the collective density oscillations, i.e., plasmon modes.

To find the dispersion of undamped plasmons, we solve $1 - v(q)\text{Re} \Pi(q, \omega) = 0$, outside the EHC. In the following,

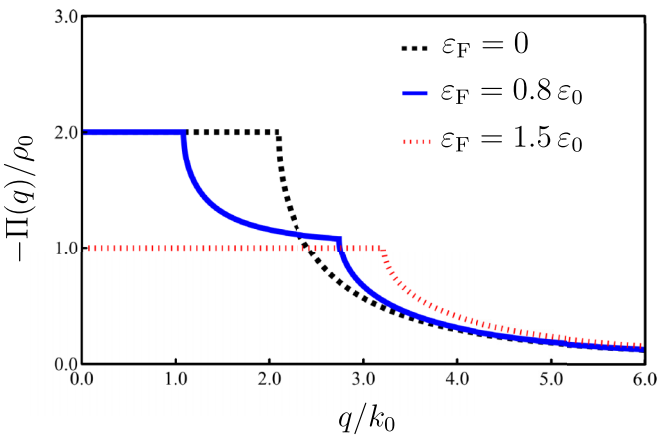


FIG. 4. Behavior of the noninteracting static polarizability of a 2D tilted NLSM (in units of $-\rho_0$) vs q/k_0 in the intrinsic (dashed black line), low-doped with $\varepsilon_F = 0.8 \varepsilon_0$ (solid blue line), and high-doped with $\varepsilon_F = 1.5 \varepsilon_0$ (dotted red line) regimes. The tilt parameter is $u = 0.3 v_0$.

we first investigate the long-wavelength behavior of plasmon modes in a 2D tilted NLSM at different doping regimes. In the $q \rightarrow 0$ limit, from [44]

$$\lim_{\omega \rightarrow 0} \lim_{q \rightarrow 0} \text{Re} \Pi(q, \omega) = \frac{\mathcal{D}}{\pi e^2} \frac{q^2}{\omega^2}, \quad (18)$$

we find

$$\omega_{\text{pl}}(q \rightarrow 0) \approx \sqrt{2\mathcal{D}q}, \quad (19)$$

where

$$\mathcal{D} = \mathcal{D}_0 \begin{cases} 2\kappa^2, & |\varepsilon_F| \leq \varepsilon_m, \\ \kappa_+^2, & |\varepsilon_F| > \varepsilon_m \end{cases} \quad (20)$$

is the Drude weight with $\mathcal{D}_0 = ge^2\varepsilon_0/2$.

Figure 6 presents the Fermi energy and tilt velocity dependence of the Drude weight. As is evident from panel (a) of Fig. 6, the Drude weight is constant for $|\varepsilon_F| < \varepsilon_m$ and linearly increases with Fermi energy for $|\varepsilon_F| > \varepsilon_m$. Panel (b) shows how the Drude weight enhances with increasing the tilt velocity at different Fermi energies. Notice that the low doping regime is defined as $|\varepsilon_F| < \varepsilon_m = \varepsilon_0(1 + u^2/v_0^2)$. Therefore, for $u > v_0\Theta(|\varepsilon_F| - \varepsilon_0)\sqrt{|\varepsilon_F|/\varepsilon_0 - 1}$, we have a topological transition in the shape of the Fermi surface. At larger tilt velocities, more curves fall into the low doping regime and merge with the blue line, which shows the intrinsic system behavior.

The Drude weight also manifests itself in the behavior of optical conductivity in the local (i.e., $q \rightarrow 0$) limit. The only contribution to the optical conductivity of our model Hamiltonian (1) arises from the intraband transitions [35]. Therefore,

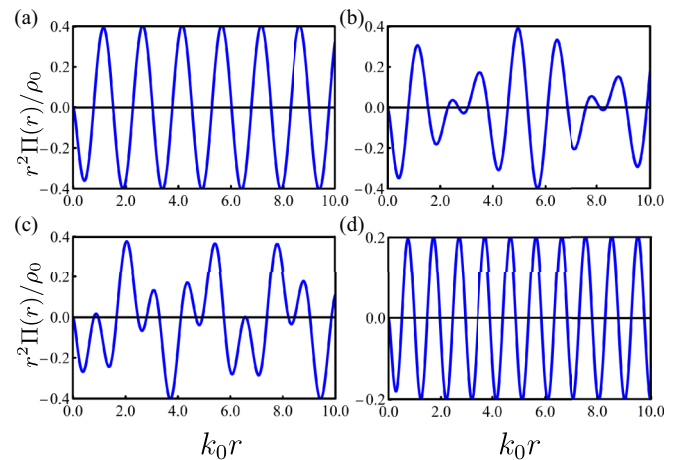


FIG. 5. The real-space static polarizability $\Pi(r)$ (in units of ρ_0/r^2) of a 2D tilted NLSM vs k_0r , at $\varepsilon_F = 0$, $\varepsilon_F = 0.3 \varepsilon_0$, $\varepsilon_F = 0.8 \varepsilon_0$, and $\varepsilon_F = 1.5 \varepsilon_0$, for panels (a), (b), (c), and (d), respectively. The tilt parameter is $u = 0.3 v_0$ in all figures.

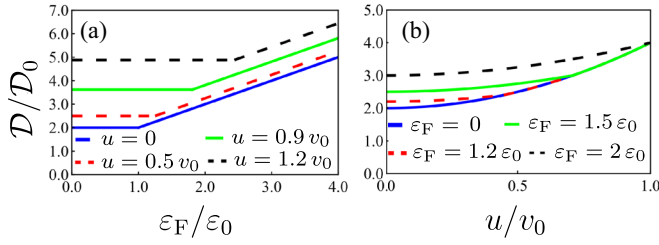


FIG. 6. The Drude weight (in units of $\mathcal{D}_0 = ge^2\varepsilon_0/2$) vs Fermi energy (a) for varying values of the tilt velocity, and (b) vs tilt velocity for varying Fermi energies.

the real part of the optical conductivity of a clean system only has the Drude peak, i.e., $\text{Re } \sigma(\omega) = \mathcal{D}\delta(\omega)$, and its imaginary part is $\text{Im } \sigma(\omega) = \mathcal{D}/(\pi\omega)$.

As we noted, the Drude weight, and therefore the plasmon dispersion to the leading order in the wave vector, is interestingly independent of the carrier concentration below a threshold density $n_m = 2\rho_0\varepsilon_m$. However, the effects of Fermi energy on the plasmon dispersion show up at larger wave vectors. Next to the leading order in q , the plasmon dispersion reads

$$\omega_{\text{pl}}(q \rightarrow 0) \approx \sqrt{2\mathcal{D}q}(1 + \gamma q + \dots), \quad (21)$$

with

$$\gamma = \frac{3a_B}{8g} \begin{cases} 1 + (\varepsilon_F/\varepsilon_m)^2, & |\varepsilon_F| \leq \varepsilon_m, \\ 2, & |\varepsilon_F| > \varepsilon_m, \end{cases} \quad (22)$$

where $a_B = 1/(me^2)$ is the effective Bohr radius. In passing, we note that two widely explored examples of two-dimensional electronic systems, i.e., the ordinary 2D electron gas with a single parabolic band (2DEG) and the Dirac fermions in a single-layer doped graphene sheet, also have a long-wavelength plasmon dispersion similar to Eq. (21). The noninteracting Drude weight in both of these systems is proportional to the Fermi energy, i.e., $\mathcal{D} = e^2\varepsilon_F$, the behavior we recover only at high doping for our 2D tilted NLSM. The coefficients of the sub-leading correction to the plasmon dispersion of 2DEG and graphene are $\gamma_{\text{2DEG}} = 3a_B/(4g)$ and $\gamma_G = -ge^2\varepsilon_F/v_F^2$, respectively, where v_F is the energy-independent Fermi velocity of graphene [45,46].

It is possible to find analytic expressions for the plasmon dispersion of 2D tilted NLSMs at arbitrary wave vectors in the intrinsic and highly doped limits as

$$\omega_{\text{pl}}(q) = \varepsilon_0 \frac{\sqrt{\bar{q}}(\eta + \bar{q})\sqrt{4\eta^2\kappa^2 + 2\eta\bar{q}^3 + \bar{q}^4}}{\eta\sqrt{2\eta + \bar{q}}} \quad (23)$$

and

$$\omega_{\text{pl}}(q) = \varepsilon_0 \frac{\sqrt{\bar{q}}(\eta + 2\bar{q})\sqrt{\eta^2\kappa_+^2 + \eta\bar{q}^3 + \bar{q}^4}}{\eta\sqrt{\eta + \bar{q}}}, \quad (24)$$

respectively, where $\bar{q} = q/k_0$ and $\eta = 2g/(k_0a_B)$. Figure 7 displays the full plasmon dispersions in three different doping regimes within the RPA. Note that we could not find an

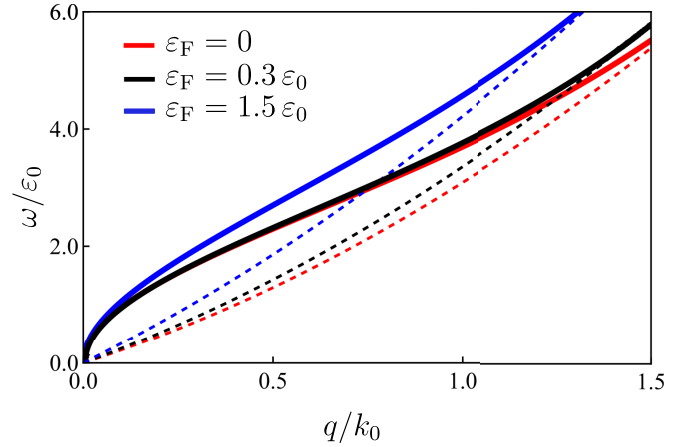


FIG. 7. Plasmon dispersion (in units of ε_0) vs q/k_0 for intrinsic $\varepsilon_F = 0$ (solid red line), low-doping with $\varepsilon_F = 0.3\varepsilon_0$ (solid black line), and high-doping with $\varepsilon_F = 1.5\varepsilon_0$ (solid blue line) 2D tilted NLSMs. The tilt velocity is fixed at $u = 0.3v_0$ and $\eta = 2g/(k_0a_B) = 4$. The upper edges of the EHC at each Fermi energy are shown with dashed lines of the same color as their corresponding plasmon dispersion curves.

analytic expression for the plasmon dispersion at arbitrary wave vectors for intermediate values of the Fermi energies. Therefore, the plasmon dispersion at $\varepsilon_F = 0.3\varepsilon_0$ (the solid black line in Fig. 7) is obtained numerically.

VI. SUMMARY AND CONCLUSION

We have investigated the linear density-density response function of two-dimensional tilted nodal-line semimetals in the intrinsic and doped regimes. Nodal-line semimetals are theoretically predicted in different two-dimensional structures, and band tilting can be induced by different means, such as external electric or magnetic fields or spin-orbit couplings originating from structural inversion asymmetry.

Despite the anisotropic band structure of the system, integration over the angular part of the wave vector \mathbf{k} washes out the anisotropy of polarizability in our simple model. Correspondingly, screening, collective mode dispersion, and optical conductivity remain isotropic at all doping levels. The origin of this isotropy lies in the absence of pseudo-spin-orbit coupling in our model system and the diagonal form of the tilt in the orbital basis. For more sophisticated tilted nodal-line models, anisotropic responses are plausible.

At low doping, two distinct singularities in the static polarizability give rise to beating patterns in the Friedel oscillations. The nodal ring radius gives the period of oscillation in the intrinsic limit. In contrast, in the doped systems, both the Fermi energy and the radius of the nodal ring contribute to the oscillation period. We also find analytical expressions for the plasmon dispersion in the intrinsic and highly doped systems. The tilt strength enhances the plasmon frequency. The collective mode frequency is proportional to $q^{1/2}$ at long wavelengths. However, the Drude weight is independent of the carrier density below a threshold carrier density.

APPENDIX A: TIGHT-BINDING MODEL OF TWO-DIMENSIONAL NODAL-LINE SEMIMETALS IN A LIEB LATTICE

As illustrated by Yang *et al.* [33], a simple three-band tight-binding model with p_z and s (or $p_{x,y}$) orbitals on a Lieb lattice can host robust two-dimensional nodal lines. Candidate materials for such structures are Be_2C and BeH_2 . In the

$$\mathcal{H}(\mathbf{k}) = \begin{pmatrix} \varepsilon_p - 2t_p[\cos(k_x a) + \cos(k_y a)] & 0 & 0 \\ 0 & \varepsilon_s & -4t_s \cos\left(\frac{k_x a}{2}\right) \cos\left(\frac{k_y a}{2}\right) \\ 0 & -4t_s \cos\left(\frac{k_y a}{2}\right) \cos\left(\frac{k_x a}{2}\right) & \varepsilon_s \end{pmatrix}, \quad (\text{A1})$$

where ε_s and ε_p are the on-site energies of s and p_z orbitals, a is the lattice constant, and $-t_s$ and $-t_p$ are the hopping amplitudes between two nearest orbitals of type s and p_z , respectively.

Diagonalizing Hamiltonian (A1), we find

$$\begin{aligned} \varepsilon_p(\mathbf{k}) &= \varepsilon_p - 2t_p[\cos(k_x a) + \cos(k_y a)], \\ \varepsilon_{s,\pm}(\mathbf{k}) &= \varepsilon_s \pm 4t_s \left| \cos\left(\frac{k_x a}{2}\right) \cos\left(\frac{k_y a}{2}\right) \right|. \end{aligned} \quad (\text{A2})$$

With a suitable choice of on-site and hopping parameters, a nodal line is formed around the Γ -point in the Brillouin zone from the intersection of $\varepsilon_p(\mathbf{k})$ and $\varepsilon_{s,+}(\mathbf{k})$ bands [33], as illustrated in Fig. 8(b).

Assuming that the Fermi energy is adjusted close to the nodal line, and concentrating on the low-energy behavior of the system, we can write an effective two-band Hamiltonian of p_z and hybrid $s + s$ orbitals,

$$\mathcal{H}(\mathbf{k}) = \begin{pmatrix} \varepsilon_p(\mathbf{k}) & 0 \\ 0 & \varepsilon_{s,+}(\mathbf{k}) \end{pmatrix} \equiv d_0(\mathbf{k})\tau_0 + d(\mathbf{k})\tau_z, \quad (\text{A3})$$

where $d_0(\mathbf{k}) = [\varepsilon_p(\mathbf{k}) + \varepsilon_{s,+}(\mathbf{k})]/2$, $d(\mathbf{k}) = [\varepsilon_p(\mathbf{k}) - \varepsilon_{s,+}(\mathbf{k})]/2$, and τ_0 and τ_z are, respectively, the 2×2 identity matrix and the z -component Pauli matrix in the pseudospin basis. Furthermore, with a simple rotation around the y -axis in the pseudospin basis, we replace $\tau_z \rightarrow \tau_x$, and then write the eigenvalues as $\varepsilon_{\pm}(\mathbf{k}) = d_0(\mathbf{k}) \pm |d(\mathbf{k})|$.

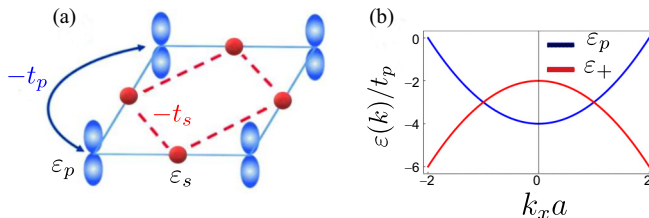


FIG. 8. (a) A Lieb lattice consisting of p_z and s orbitals. (b) The tight-binding band dispersion of $\varepsilon_p(k)$ and $\varepsilon_{s,+}(k)$ bands vs k_x for $k_y = 0$, and at the vicinity of the band touching point. We have used $\varepsilon_s - \varepsilon_p = 10t_p$ and $t_s = 2t_p$ for on-site and hopping parameters, respectively.

following, we discuss only the lattice model with one p_z and two s orbitals at each unit cell [see Fig. 8(a)] as a representative model for the 2D NLSM, but similar conclusions could be drawn from other models.

The orthogonality of p_z and s orbitals at different sites prevents nearest-neighbor hopping. If we consider the next-nearest-neighbor hoppings (for every sublattice), the tight-binding Hamiltonian in momentum space reads

In the low-energy (i.e., $\mathbf{k} \rightarrow \mathbf{0}$) limit, we have

$$\begin{aligned} d_0(\mathbf{k} \rightarrow \mathbf{0}) &\approx \frac{\varepsilon_s + \varepsilon_p}{2} + 2(t_s - t_p) \\ &\quad + \frac{1}{2}(t_p - t_s/2)k^2 a^2 + O(k^4), \\ d(\mathbf{k} \rightarrow \mathbf{0}) &\approx -\frac{\varepsilon_s - \varepsilon_p}{2} - 2(t_s + t_p) \\ &\quad + \frac{1}{2}(t_p + t_s/2)k^2 a^2 + O(k^4). \end{aligned} \quad (\text{A4})$$

For $t_s \approx 2t_p$, $d_0(\mathbf{k} \rightarrow \mathbf{0})$ becomes independent of the wave vector (up to the quadratic order k) and represents the constant energy of the band crossing point, and we find

$$\mathcal{H}(\mathbf{k} \rightarrow \mathbf{0}) \approx d(\mathbf{k} \rightarrow \mathbf{0})\tau_x \approx \frac{1}{2m^*}(k^2 - k_0^2)\tau_x, \quad (\text{A5})$$

where we have defined $1/m^* = a^2(t_p + t_s/2)$ and $k_0^2 = m^*[\varepsilon_s - \varepsilon_p + 4(t_s + t_p)]$.

Up to now, we had forgotten about the real spin degree of freedom, and the bands we obtained were spin-degenerate. The nodal line can get tilted through either inversion or time-reversal symmetry breaking. The effects of structural inversion asymmetry appear as a spin-orbit coupling term [47],

$$H_{\text{SOC}} = \alpha(\mathbf{k} \times \mathbf{E}) \cdot \boldsymbol{\sigma}, \quad (\text{A6})$$

where α is the strength of spin-orbit coupling, $\boldsymbol{\sigma}$ is the vector of Pauli matrices acting on real spin, and \mathbf{E} is an electric field resulting from the structural inversion asymmetry. An in-plane electric field $\mathbf{E} = (E_x, E_y, 0)$ produces a linear tilt term in the nodal-line Hamiltonian as $(\mathbf{u} \cdot \mathbf{k})\sigma_z$, where $\mathbf{u} = \alpha(E_y, -E_x, 0)$ is the tilt velocity vector, and up and down spin subbands are tilted in opposite directions because of σ_z .

APPENDIX B: DETAILS OF CALCULATING THE DYNAMICAL POLARIZABILITY

The dynamical polarizability of the 2D NLSM could be obtained from Eq. (5), and we use the identity $\lim_{\eta \rightarrow 0^+} 1/(x + i\eta) = \text{P}(1/x) - i\pi\delta(x)$ to find its real and imaginary parts.

It is more convenient to calculate the imaginary part of the polarizability first and then use the Kramers-Kronig relation to obtain the real component. Making use of the Dirac δ function to eliminate the integration over k_y , we find

$$\text{Im } \Pi(\mathbf{q}, \omega) = \frac{-\rho_0}{q^2 |q_y|} \sum_{s,s'=\pm 1} \sum_{\lambda=\pm} \int_{-\infty}^{\infty} dk_x \Theta(sA_\lambda) \Theta(s'B_\lambda) \times [\Theta(C_\lambda + \varepsilon_F) - \Theta(C_\lambda + \varepsilon_F - \omega)], \quad (\text{B1})$$

where we have used the following definitions:

$$\begin{aligned} A_+(k_x) &= - \left[1 + \left(\frac{q_x}{q_y} \right)^2 \right] k_x^2 + \left(\frac{f_+ q_x}{q_y^2} \right) k_x - \frac{f_+^2}{4q_y^2} + 1, \\ A_-(k_x) &= \left[1 + \left(\frac{q_x}{q_y} \right)^2 \right] k_x^2 - \left(\frac{f_- q_x}{q_y^2} \right) k_x + \frac{f_-^2}{4q_y^2} - 1, \\ B_+(k_x) &= A_+ - q^2 - f_+, \\ B_-(k_x) &= A_- + q^2 + f_-, \\ C_\pm(k_x) &= -A_\pm - uk_x, \end{aligned} \quad (\text{B2})$$

with $f_\pm = \pm(2uq_x - \omega) - q^2$. In the above equation, for convenience, we used the dimensionless quantities in which all energies, velocities, and wave vectors are expressed in units of ε_0 , v_0 , and k_0 , respectively. Now, performing the summation over the band indices in Eq. (B1), and noting that

$\Theta(-x) = 1 - \Theta(x)$, we arrive at

$$\text{Im } \Pi(\mathbf{q}, \omega) = \frac{-\rho_0}{q^2 |q_y|} \sum_{\lambda=\pm} \int_{-\infty}^{\infty} dk_x [\Theta(C_\lambda(k_x) + \varepsilon_F) \times -\Theta(C_\lambda(k_x) + \varepsilon_F - \omega)]. \quad (\text{B3})$$

Considering the arguments of the above four step-functions that are quadratic functions of k_x , 16 regions can be defined, but only the following five regions,

$$\begin{aligned} \text{I: } & \Delta_1 > 0; \Delta_2 > 0; \Delta_3 > 0; \Delta_4 > 0, \\ \text{II: } & \Delta_1 < 0; \Delta_2 > 0; \Delta_3 > 0; \Delta_4 > 0, \\ \text{III: } & \Delta_1 < 0; \Delta_2 > 0; \Delta_3 > 0; \Delta_4 < 0, \\ \text{IV: } & \Delta_1 < 0; \Delta_2 < 0; \Delta_3 > 0; \Delta_4 > 0, \\ \text{V: } & \Delta_1 < 0; \Delta_2 < 0; \Delta_3 > 0; \Delta_4 < 0, \end{aligned} \quad (\text{B4})$$

give nonzero contributions to the integrand in Eq. (B3), where $\Delta_1 = \kappa_-^2 - v_+^2$, $\Delta_2 = \kappa_+^2 - v_-^2$, $\Delta_3 = \kappa_-^2 - v_-^2$, and $\Delta_4 = \kappa_+^2 - v_+^2$ are the discriminants of four quadratic functions of k_x , i.e., $C_+(k_x) + \varepsilon_F$, $C_-(k_x) + \varepsilon_F$, $C_+(k_x) + \varepsilon_F - \omega$, and $C_-(k_x) + \varepsilon_F - \omega$, respectively, and κ_\pm and v_\pm are defined in the main text. By determining the sign of the functions and solving the integral over k_x in Eq. (B3), we arrive at Eq. (9).

The real parts of the polarizability can be obtained from the imaginary parts using the Kramers-Kronig relation. The procedure is straightforward and results in Eq. (10).

Note that for vanishing Fermi energy, where $\Delta_1 = \Delta_4$ and $\Delta_2 = \Delta_3$, regions II, IV, and V do not exist, and we find two regions corresponding to the EHC of an undoped system.

-
- [1] X.-L. Qi and S.-C. Zhang, Topological insulators and superconductors, *Rev. Mod. Phys.* **83**, 1057 (2011).
- [2] Y. Xia, D. Qian, D. Hsieh, L. Wray, A. Pal, H.-H. Lin, A. Bansil, D. Grauer, Y. Hor, R. Cava, and M. Z. Hasan, Observation of a large-gap topological-insulator class with a single Dirac cone on the surface, *Nat. Phys.* **5**, 398 (2009).
- [3] M. Z. Hasan and C. L. Kane, Colloquium: Topological insulators, *Rev. Mod. Phys.* **82**, 3045 (2010).
- [4] A. Burkov, Topological semimetals, *Nat. Mater.* **15**, 1145 (2016).
- [5] N. P. Armitage, E. J. Mele, and A. Vishwanath, Weyl and Dirac semimetals in three-dimensional solids, *Rev. Mod. Phys.* **90**, 015001 (2018).
- [6] A. P. Schnyder, *Topological semimetals*, in *Topology, Entanglement, and Strong Correlations*, Schriften des Forschungszentrums Jülich, Reihe Modeling and Simulation Vol. 10, edited by E. Pavarini and E. Koch, Autumn School on Correlated Electrons (Forschungszentrum Jülich GmbH Zentralbibliothek, Verlag, Jülich, 2020).
- [7] S. M. Young, S. Zaheer, J. C. Y. Teo, C. L. Kane, E. J. Mele, and A. M. Rappe, Dirac semimetal in three dimensions, *Phys. Rev. Lett.* **108**, 140405 (2012).
- [8] B.-J. Yang and N. Nagaosa, Classification of stable three-dimensional Dirac semimetals with nontrivial topology, *Nat. Commun.* **5**, 4898 (2014).
- [9] A. A. Burkov and L. Balents, Weyl semimetal in a topological insulator multilayer, *Phys. Rev. Lett.* **107**, 127205 (2011).
- [10] X. Wan, A. M. Turner, A. Vishwanath, and S. Y. Savrasov, Topological semimetal and Fermi-arc surface states in the electronic structure of pyrochlore iridates, *Phys. Rev. B* **83**, 205101 (2011).
- [11] Z. Liu, B. Zhou, Y. Zhang, Z. Wang, H. Weng, D. Prabhakaran, S.-K. Mo, Z. Shen, Z. Fang, X. Dai, Z. Hussain, and Y. Chen, Discovery of a three-dimensional topological Dirac semimetal, Na_3Bi , *Science* **343**, 864 (2014).
- [12] Z. Wang, H. Weng, Q. Wu, X. Dai, and Z. Fang, Three-dimensional Dirac semimetal and quantum transport in Cd_3As_2 , *Phys. Rev. B* **88**, 125427 (2013).
- [13] S.-Y. Xu, I. Belopolski, N. Alidoust, M. Neupane, G. Bian, C. Zhang, R. Sankar, G. Chang, Z. Yuan, C.-C. Lee, S.-M. Huang, H. Zheng, J. Ma, D. Sanchez, B. Wang, A. Bansil, F. Chou, P. Shibaev, H. Lin, and M. Z. Hasan, Discovery of a Weyl fermion semimetal and topological Fermi arcs, *Science* **349**, 613 (2015).
- [14] H. Weng, C. Fang, Z. Fang, B. A. Bernevig, and X. Dai, Weyl semimetal phase in noncentrosymmetric transition-metal monophosphides, *Phys. Rev. X* **5**, 011029 (2015).
- [15] A. Soluyanov, D. Gresch, Z. Wang, Q.-S. Wu, M. Troyer, X. Dai, and B. Bernevig, Type-II weyl semimetals, *Nature (London)* **527**, 495 (2015).

- [16] X.-P. Li, K. Deng, B. Fu, Y. K. Li, D.-S. Ma, J. F. Han, J. Zhou, S. Zhou, and Y. Yao, Type-III weyl semimetals: $(\text{TaSe}_4)_2\text{I}$, *Phys. Rev. B* **103**, L081402 (2021).
- [17] C.-Y. Tan, J.-T. Hou, C.-X. Yan, H. Guo, and H.-R. Chang, Signatures of Lifshitz transition in the optical conductivity of two-dimensional tilted Dirac materials, *Phys. Rev. B* **106**, 165404 (2022).
- [18] A. Hosseinzadeh and S. A. Jafari, Semiclassical transport in two-dimensional Dirac materials with spatially variable tilt, [arXiv:2303.06030](https://arxiv.org/abs/2303.06030).
- [19] Z. Jalali-Mola and S. A. Jafari, Tilt-induced many-body corrections to optical conductivity of tilted Dirac cone materials, *Phys. Rev. B* **104**, 085152 (2021).
- [20] Z. Faraei and S. A. Jafari, Electrically charged Andreev modes in two-dimensional tilted Dirac cone systems, *Phys. Rev. B* **101**, 214508 (2020).
- [21] C. Fang, H. Weng, X. Dai, and Z. Fang, Topological nodal line semimetals, *Chin. Phys. B* **25**, 117106 (2016).
- [22] C. Fang, Y. Chen, H.-Y. Kee, and L. Fu, Topological nodal line semimetals with and without spin-orbital coupling, *Phys. Rev. B* **92**, 081201(R) (2015).
- [23] R. Yu, H. Weng, Z. Fang, X. Dai, and X. Hu, Topological node-line semimetal and Dirac semimetal state in antiperovskite Cu_3PdN , *Phys. Rev. Lett.* **115**, 036807 (2015).
- [24] X.-B. Wang, X.-M. Ma, E. Emmanouilidou, B. Shen, C.-H. Hsu, C.-S. Zhou, Y. Zuo, R.-R. Song, S.-Y. Xu, G. Wang, L. Huang, N. Ni, and C. Liu, Topological surface electronic states in candidate nodal-line semimetal CaAgAs , *Phys. Rev. B* **96**, 161112(R) (2017).
- [25] M. B. Schilling, L. M. Schoop, B. V. Lotsch, M. Dressel, and A. V. Pronin, Flat optical conductivity in ZrSiS due to two-dimensional Dirac bands, *Phys. Rev. Lett.* **119**, 187401 (2017).
- [26] A. Topp, R. Queiroz, A. Grüneis, L. Mühler, A. W. Rost, A. Varykhalov, D. Marchenko, M. Krivenkov, F. Rodolakis, J. L. McChesney, B. V. Lotsch, L. M. Schoop, and C. R. Ast, Surface floating 2D bands in layered nonsymmorphic semimetals: ZrSiS and related compounds, *Phys. Rev. X* **7**, 041073 (2017).
- [27] Y. Shao, Z. Sun, Y. Wang, C. Xu, R. Sankar, A. J. Breindel, C. Cao, M. M. Fogler, A. J. Millis, F. Chou, Z. Li, T. Timusk, M. B. Maple, and D. N. Basov, Optical signatures of Dirac nodal lines in NbAs_2 , *Proc. Natl. Acad. Sci. USA* **116**, 1168 (2019).
- [28] Z. Qiu, C. Le, Z. Liao, B. Xu, R. Yang, J. Hu, Y. Dai, and X. Qiu, Observation of a topological nodal-line semimetal in YbMnSb_2 through optical spectroscopy, *Phys. Rev. B* **100**, 125136 (2019).
- [29] C. Chen, X. Xu, J. Jiang, S.-C. Wu, Y. P. Qi, L. X. Yang, M. X. Wang, Y. Sun, N. B. M. Schröter, H. F. Yang, L. M. Schoop, Y. Y. Lv, J. Zhou, Y. B. Chen, S. H. Yao, M. H. Lu, Y. F. Chen, C. Felser, B. H. Yan, Z. K. Liu *et al.*, Dirac line nodes and effect of spin-orbit coupling in the nonsymmorphic critical semimetals $M\text{SiS}$, ($M = \text{Hf}, \text{Zr}$), *Phys. Rev. B* **95**, 125126 (2017).
- [30] Y. Shao, A. Rudenko, J. Hu, Z. Sun, Y. Zhu, S. Moon, A. Millis, S. Yuan, A. Lichtenstein, D. Smirnov, Z. Mao, M. Katsnelson, and D. Basov, Electronic correlations in nodal-line semimetals, *Nat. Phys.* **16**, 636 (2020).
- [31] J. Yuanjun, R. Wang, J. Zhao, C. Zheng, L.-Y. Gan, J. Liu, H. Xu, and S. Tong, A family group of two-dimensional node-line semimetals, *Nanoscale* **9**, 13112 (2016).
- [32] J.-L. Lu, W. Luo, X.-Y. Li, S.-Q. Yang, J. Cao, X.-G. Gong, and H. Xiang, Two-dimensional node-line semimetals in a honeycomb-Kagome lattice, *Chin. Phys. Lett.* **34**, 057302 (2016).
- [33] B.-J. Yang, X. Zhang, and M. Zhao, Dirac node lines in two-dimensional Lieb lattices, *Nanoscale* **9**, 8740 (2017).
- [34] C. Ding, H. Gao, W. Geng, and M. Zhao, Anomalous plasmons in a two-dimensional Dirac nodal-line Lieb lattice, *Nanoscale Adv.* **3**, 1127 (2021).
- [35] S. Barati and S. H. Abedinpour, Optical conductivity of three and two dimensional topological nodal-line semimetals, *Phys. Rev. B* **96**, 155150 (2017).
- [36] S. Ahn, E. J. Mele, and H. Min, Electrodynamics on Fermi cyclides in nodal line semimetals, *Phys. Rev. Lett.* **119**, 147402 (2017).
- [37] S. Barati and S. H. Abedinpour, Thermoelectric response of nodal-line semimetals: Probing the Fermi surface topology, *Phys. Rev. B* **102**, 125139 (2020).
- [38] Z. Yan, P.-W. Huang, and Z. Wang, Collective modes in nodal line semimetals, *Phys. Rev. B* **93**, 085138 (2016).
- [39] J.-W. Rhim and Y. B. Kim, Anisotropic density fluctuations, plasmons, and Friedel oscillations in nodal line semimetal, *New J. Phys.* **18**, 043010 (2016).
- [40] J. Cao, H.-R. Chang, X. Feng, Y. Yao, and S. A. Yang, Plasmons in a two-dimensional nonsymmorphic nodal-line semimetal, *Phys. Rev. B* **107**, 115168 (2023).
- [41] J. Ekström, E. H. Hasdeo, M. B. Farias, and T. L. Schmidt, Kerr effect in tilted nodal loop semimetals, *Phys. Rev. B* **104**, 125411 (2021).
- [42] A. Martín-Ruiz and A. Cortijo, Parity anomaly in the nonlinear response of nodal-line semimetals, *Phys. Rev. B* **98**, 155125 (2018).
- [43] G. Giuliani and G. Vignale, *Quantum Theory of the Electron Liquid* (Cambridge University Press, Cambridge, 2005).
- [44] S. H. Abedinpour, G. Vignale, A. Principi, M. Polini, W.-K. Tse, and A. H. MacDonald, Drude weight, plasmon dispersion, and ac conductivity in doped graphene sheets, *Phys. Rev. B* **84**, 045429 (2011).
- [45] E. H. Hwang and S. Das Sarma, Dielectric function, screening, and plasmons in two-dimensional graphene, *Phys. Rev. B* **75**, 205418 (2007).
- [46] F. Stern, Polarizability of a two-dimensional electron gas, *Phys. Rev. Lett.* **18**, 546 (1967).
- [47] R. Winkler, *Spin-Orbit Coupling Effects in Two-Dimensional Electron and Hole Systems*, Springer Tracts in Modern Physics Vol. 191 (Springer, Berlin, 2003).